Low-frequency phonon modes in layered silver-bismuth double perovskites: symmetry, polarity, and relation to phase transitions

Beatriz Martín-García*†, Davide Spirito*†, Miao-Ling Lin, Yu-Chen Leng, Sergey Artyukhin, Ping-Heng Tan, Roman Krahne*

((Optional Dedication))

B. Martín-García
CIC nanoGUNE, Tolosa Hiribidea, 76, 20018 Donostia-San Sebastian, Basque Country
(Spain) (b.martingarcia@nanogune.eu)
D. Spirito
IHP–Leibniz-Institut für innovative Mikroelektronik, Im Technologiepark 25, 15236 Frankfurt
(Oder), Germany (spirito@ihp-microelectronics.com)
M-L. Lin, Y-C. Leng, P-H. Tan
State Key Laboratory of Superlattices and Microstructures, Institute of Semiconductors,
Chinese Academy of Sciences, 100083 Beijing, China
Center of Materials Science and Optoelectronics Engineering, University of Chinese
Academy of Sciences, 100190 Beijing, China
S. Artyukhin, R. Krahne
Istituto Italiano di Tecnologia, Via Morego 30, 16163 Genova (Italy) (roman.krahne@iit.it)

ABSTRACT Metal halide perovskites are emergent materials for a large range of applications, and the layered double perovskite architectures vastly enrich the opportunities to design their composition, structural properties, and optoelectronic behavior. The stability, crystal phase, and electronic band gap depend strongly on the bonds and distortions of the octahedra lattice that are at the origin of the vibrational spectrum of these materials. Here we investigate the structural dynamics of flakes of exfoliated layered Ag/Bi bromide double perovskites by angle-dependent polarized Raman spectroscopy and density-functional theory modeling. The well-defined orientation of the inorganic octahedra lattice with respect to the light polarization allows to correlate the angle-dependent intensity of the Raman signal to the directionality and symmetry

1

of the phonon modes. We reveal low frequency vibrations and provide a detailed microscopic and group theory assignment of the Raman modes. The temperature-dependent measurements across the phase transitions show marked changes in the phonon frequencies, reveal soft modes, and allow to distinguish first from second order transitions as well as determine their transition temperature. This provides highly valuable insights to improve the properties of this class of Pb-free perovskites for applications in energy harvesting and optoelectronics.

1. Introduction

Metal halide double perovskites are receiving an increasing attention as more environmentally friendly and stable alternatives to the Pb-based perovskites (PSKs).[1] Although they do not yet reach the high performance of their Pb counterparts in optoelectronic devices, recent efforts, particularly on $Cs_2AgBiBr_6$ double PSK,[2] demonstrate their potential use in a broad range of applications from solar cells,[3–9] photodetectors,[10,11] X-Ray detectors,[12] memristors[13] to photocatalysts[14]. Moreover, when passing from the 3D double PSK toward its layered counterparts with two (2L) or one (1L) octahedra layers by introducing large A-site organic cations, such as butylammonium (BA) or propylammonium (PA), allowed to develop new low-dimensional (2D) materials with tunable optoelectronic properties, such as the character of the bandgap as well as the bandgap energy from ~2 eV to ~3 eV, which is related to the distortion of the inorganic lattice.[15–19] The dimensional reduction also improved remarkably the ON/OFF ratio of memristors from 10^2 ($Cs_2AgBiBr_6$ – 3D) up to 10^7 (($BA)_2CsAgBiBr_7$), since in distorted crystal structures the ion migration is favored.[20] X-Ray photodetectors from (($BA)_2CsAgBiBr_7$ with large mobility-lifetime product were obtained, where the sensitivity depends on the dimensionality of the crystal (number of octahedral layers).[21,22] The time-response of photodetectors could be enhanced through dimensional reduction, while keeping a similar detectivity;[23] and in ($PA)_2CsAgBiBr_7$ its layered structure leads also to strong-polarization sensitivity [24]. The examples above demonstrate that the crystal structure determines the band gap, exciton binding energy, density of trap states and more, and

therefore governs the optoelectronic properties, emphasizing the need of a detailed study of the structural dynamics. While the optical properties were extensively studied, showing indirect bandgap and large electron-phonon coupling strength in 3D $Cs_2AgBiBr_6$,[25–31] the structural dynamics have received less attention[25,26,30,32]. This is even more true for the structural dynamics in layered Ag/Bi-based double perovskites, for which we studied the high-frequency modes by Raman spectroscopy in a previous work, evidencing the impact of the organic cations in phase transitions. [33] However, for the optoelectronic properties the vibrational modes of the inorganic perovskite lattice in the low-frequency range are particularly relevant, as has been demonstrated for 3D[34–38] and layered[39–43] PSKs, and the properties of these vibrational modes have not been investigated in the double perovskites so far.

In this work, we investigate the vibrational properties of a family of Ag/Bi double perovskites comprising 3D bulk crystals and the layered structures with one (1L) and two (2L) inorganic metal halide layers. Angle-dependent polarized Raman spectroscopy enables a detailed analysis of the symmetries of the basic phonon modes, which is combined with symmetry assignment by group theory and insight on the vibrational motions by density functional theory (DFT) modeling. This allows to distinguish modes with "isotropic", "dipolar", and "quadrupolar" modes in their angular dependence, and to assign them to vibrations of the octahedra cages, the inorganic metal-halide lattice bonds, and/or coupling to the organic cations in the case of the 1L and 2L structures. We focus our study on the low-frequency range of 8-200 cm^{-1} where the phonon bands of the inorganic lattice are located, and present the detailed Raman mode spectrum for the 3D, 2L and 1L Ag/Bi double perovskites for both their room temperature (RT, taken as 300K) and low temperature phases. Our access to the ultralow-frequency range allowed us to reveal two bands in the 3D structure that have not been reported before, appearing at ~18 and ~29 cm^{-1} in the low-temperature tetragonal phase. Concerning the 1L and 2L structures, we present the first study of the low frequency Raman bands (below 80 cm^{-1}), where we identify

a wealth of Raman active bands that can be related to octahedra motions and metal-Br bond stretching or bending. Interestingly, we find some soft modes that appear only in the low-temperature phase and for which their frequency decreases markedly with increasing temperature. Mapping the temperature behavior and the symmetry of the phonon modes allows to clearly identify the phase transition temperature in our samples, and provides additional insights if the phase transition consists of a first order process involving structural changes of the inorganic lattice, or second order ones that stem from order/disorder transition in the organic layers.

2. Results and Discussion

Figure 1 shows optical microscope images of the double perovskite crystals that are investigated by Raman spectroscopy and DFT modeling in this work, together with cross section views of their crystal structure illustrating their room and low temperature phases. The 3D crystals grow forming a kind of truncated cube (**Figure 1** and see **SI**, **Figure S1**), providing optical access to their (111) facet as flat surface, and are in cubic phase at RT and tetragonal phase below 120K.[26] For the low-dimensional layered structures we mechanically exfoliated single flakes with the (001) plane parallel to the SiO_2/Si substrate surface. For the 2L-BA and 1L-BA layered samples the structure is monoclinic both at RT and low temperature, however, in the range 100-298K for 2L-BA[15] and ~282K for 1L-BA[33] there is a conformational order to disorder rearrangement of the organic cations accompanied by a change in the octahedral tilting (angle and bonds distortion) inside the inorganic lattice (Figure 1b,c), leading to a phase transition of the whole crystal structure. The optical and structural properties (temperature-dependent absorption and photoluminescence and x-ray diffraction) of the crystals were reported in ref. [33].
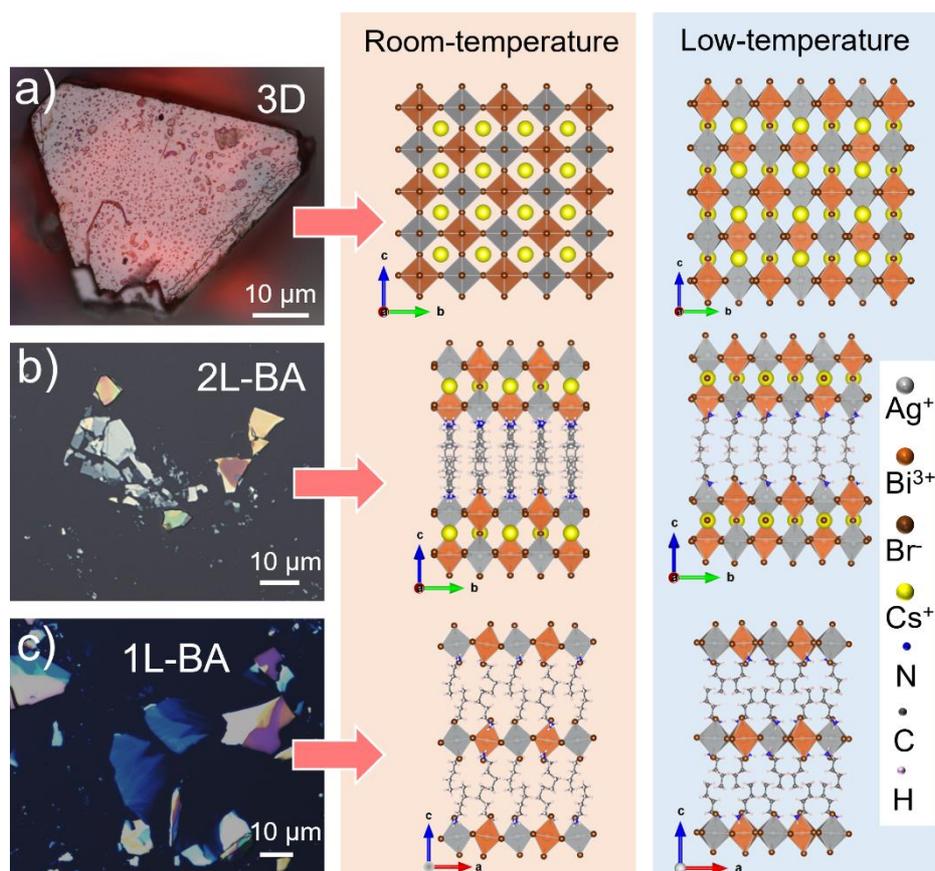
Figure 1. Optical microscope images of the different double perovskite structures: (a) 3D $Cs_2AgBiBr_6$ microcrystals and mechanically exfoliated 2L-BA (b) and 1L-BA (c) flakes on SiO_2/Si substrates together with their crystal structures drawn using VESTA 3 software[44] based on the crystallographic data from refs. [15,26].

Figure 2 shows unpolarized Raman spectra recorded at room temperature and 30K for all samples, thus above and below the phase transitions, together with the results from DFT modeling of the Raman active modes at 0K. For all three double-perovskite structures, the room temperature Raman spectra are dominated by a high-frequency mode around 170 cm^{-1}, that is slightly red-shifted in the layered structures by varying the number of octahedral layers, in agreement with literature[33]. Furthermore, a strong mode at 73 cm^{-1} is observed in the 3D sample, while the 2L and 1L structures show multiple peaks in the low-frequency range below 100 cm^{-1}. The low-temperature Raman spectra reveal a much more complex response, with

different sets of phonon modes in the low-frequency regime. This marked difference between room and low temperature spectra can be attributed to the crystal phase transition (at 122K, 100-298K, and 282 K for 3D,[26] 2L[15] and 1L[33] structures, respectively), and because of the drastically reduced thermal noise and broadening at low temperatures that allow to resolve weak and narrow phonon bands. The low temperature Raman spectra can be compared with DFT modeling at 0K (see details in Section 2 in the SI), where the Raman active modes (stemming from optical phonons), their symmetry, and their relative intensities are shown in the bottom row of Figure 2. Furthermore, in the DFT modeling a depolarization factor D can be defined as the ratio of the polarized (∥) and depolarized (⊥) intensities averaged over the incidence angle. This D can be assigned to the vibrations of the ionic lattice that allows to classify the modes into "isotropic", "dipolar", and "quadrupolar" ones, as detailed in the caption of Figure 2. We established this notation according to the angle-dependence of the Raman modes in the polar plots discussed in detail later (Figures 4-6). We note that passing from 3D to 2D layered compounds leads to a reduction in symmetry of the system, which changes the point group from C_{4h} (for 3D) to C_2 (for 2L-BA) and C_{2h} (for 1L-BA).[15,26] Overall, we find a good agreement between the experimental data and DFT modeling, which allows us to analyze the vibrational motions of the dominant modes in those crystal structures.

The dominant phonon mode around 170 cm^{-1} that is observed in all experimental spectra is isotropic and A_{1g} -like. It is typically attributed to the LO phonon mode and dominated by out-of-plane oscillation components. Then, the 3D crystals have two more pronounced modes around 140 cm^{-1} and 75 cm^{-1} that have E_g symmetry.[25,30] Furthermore, we observe at low temperature a set of four peaks at 18, 29, 40, and 45 cm^{-1} that we assign to rocking and/or twisting motions in the $[AgBr_6]^{5-}$ and $[BiBr_6]^{3-}$ octahedra, which is in line with ref [30] and the interpretation of the lowest energy modes in lead-halide perovskites[45]. The low-frequency range of the 1L-BA and 2L-BA samples features a much larger set of peaks with different symmetries that will be discussed in detail later on.
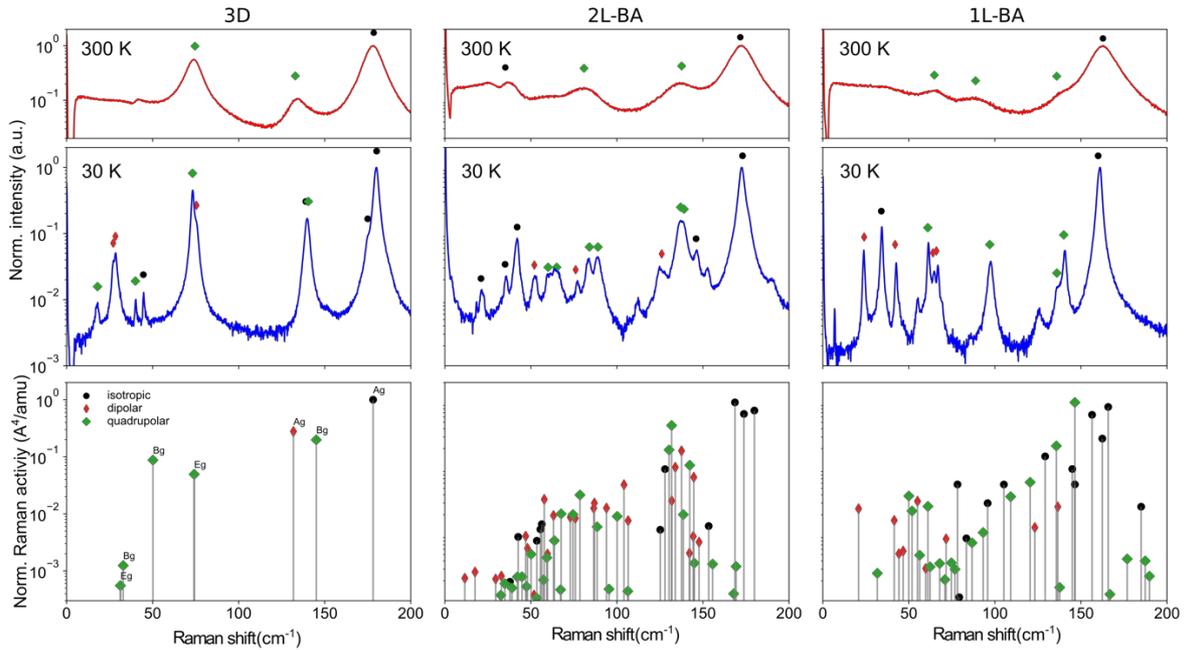
Figure 2. Comparison of the experimental Raman spectra using y-axis logarithmic scale for highlighting the low-intensity modes and DFT results for 3D, 2L-BA and 1L-BA samples. Experimental data are unpolarized spectra measured at RT and 30K (shown on semi-log scale), normalized to the strongest peak. The DFT modeling results are displayed in terms of Raman frequency and activity. The symbols mark the polarization of the modes that are defined by the depolarization factor D, classified as "isotropic" for D<0.15, "dipolar" for 0.15<D<0.72, and "quadrupolar" for D>0.72.

To get deeper insight into the symmetries of the phonon modes we performed angle-dependent polarized Raman spectroscopy, which allows to correlate the linear polarization in excitation (polarizer) and detection (analyzer) with the orientation of the 2D lattice under investigation. Here the rotation of the linearly polarized light in the combined excitation/detection path (see Experimental Methods in SI) with a $\lambda/2$ wave plate by an angle of $\theta/2$ is equivalent to the rotation of the sample reference frame by an angle θ to the reference frame of the linear polarizers. Therefore we can interpret the data as if the orientation of the linear polarizers, which

are parallel (polarized) or orthogonal (depolarized), is rotated with respect sample.[46] Such investigation of the Raman modes with well-defined light polarization with respect to the lattice orientation of the sample provides detailed insight into the underlying symmetries of the phonon bands and the directionality of the vibrations in the ionic octahedra lattice.

However, before we present such analysis in detail for the 2L-BA and 1L-BA structures, we will discuss our angle-dependent Raman results of the 3D crystals, that due to the (111) surface facet does not provide octahedra lattice plane at orthogonal angles to the light polarization or pointing vector.

Figure 3a shows the view on one octahedra lattice plane of the 3D structure from the diagonal direction that corresponds to the exposed (111) surface plane. We note that this geometry does not allow a straightforward assignment of phonon symmetries, because the light polarization is diagonal to the in-plane and out-of-plane components in the octahedra lattice. Nevertheless, we observe an angle-dependence of the Raman intensity for some modes, in particular for the low-frequency modes at 18, 29, 40 and 45 cm^{-1} at low temperature in both polarized and depolarized measurements. This illustrates that the relative intensity of Raman-active modes measured from single crystals can strongly depend on the experimental configuration. The other modes that we observe at 73 and 140 cm^{-1} have roughly constant intensity regardless of the rotation angle of the polarization, and the LO phonon mode at 180 cm^{-1} manifests an angle dependence only in depolarized measurements. We present a symmetry analysis based on the Raman tensor in such a rotated system in Section 5.2 in the SI.
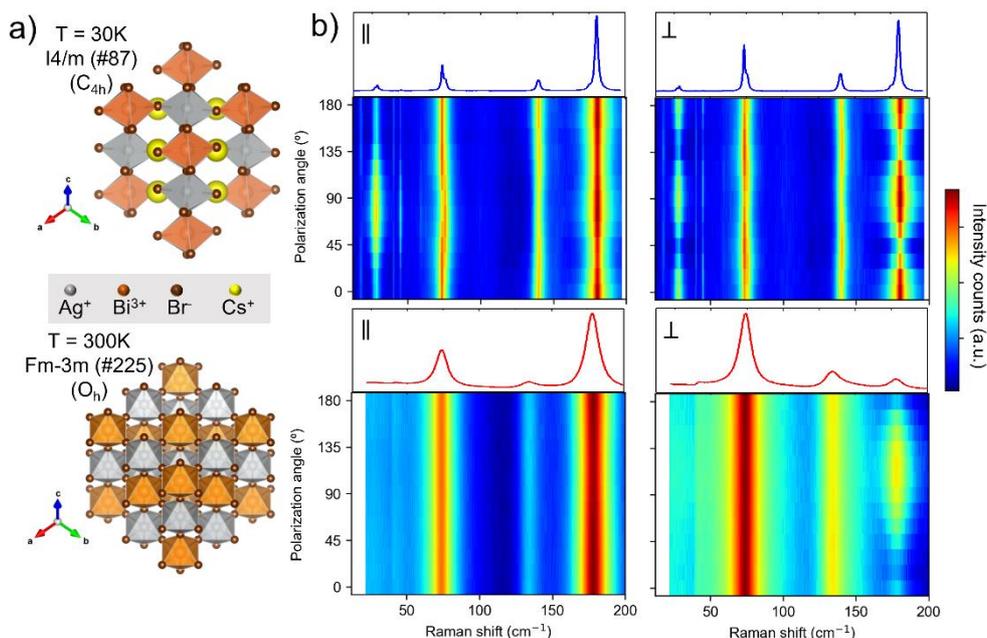
Figure 3. (a) Crystal structures of the 3D $Cs_2AgBiBr_6$ PSK drawn using VESTA software[44] for the low- and high-temperature phases[26] from the perspective of the (*111*) plane that is exposed in the experiment. (b) Color plots of the angle dependence of the Raman spectrum for polarized (∥) and depolarized (⊥) configurations. The integrated Raman spectra along the polarization angle are shown on top of the color plots.

We now turn to the layered double perovskites 2L-BA and 1L-BA structures. Here the exfoliated flakes have their (001) plane parallel to the substrate, and therefore we can straightforwardly relate the angle-dependence of the Raman-active modes to the crystal symmetries. For a facile overview of the behavior of the different modes we will use polar plots of the angle-dependent intensity of the different Raman modes. Such a polar plot is sketched in Scheme 1 together with the fixed orientation of the octahedra lattice, where the angle corresponds to the direction of the light polarization, and the radius to the normalized angle dependent intensity of the mode.
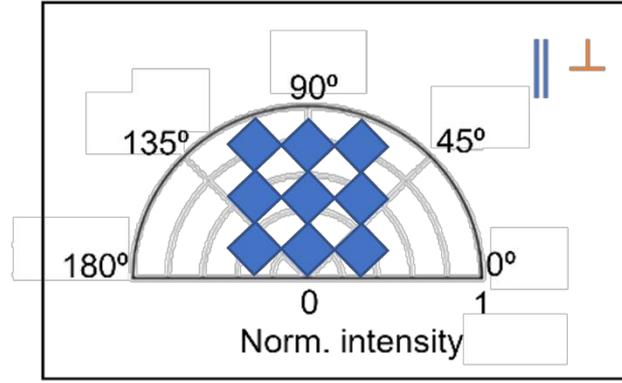
Scheme 1. Polar plot scheme where the angle gives the direction of the light polarization with respect to the fixed frame of the octahedra lattice (sketched by the array of blue squares) of the sample. The normalized mode intensity is given by the length of the radial coordinate.

The intensity of a Raman mode is given by $\left|\vec{e_i}\overleftrightarrow{R}\vec{e_s}\right|^2$, e_s and e_i being the polarization of scattered and incident light, and the Raman tensor R. As in our experimental configuration, the incidence is along the z-axis, and the collected light is polarized in the xy-plane. For non-resonant excitation, the Raman tensor is

$$\overleftrightarrow{R} = \begin{pmatrix} a & d & \cdot \\ d & b & \cdot \\ \cdot & \cdot & \cdot \end{pmatrix}$$

where the coefficients related to polarization along z are replaced by a dot.

Figure 4a shows the calculated angular dependence of the Raman intensity for different values of a,b,d that result in different symmetries (see Section 5 in the SI for details on the calculation). We find an isotropic A_{1g}-like mode for a diagonal Raman tensor with $a = b$. Dipolar (red) and quadrupolar (green/brown) modes are obtained for other combinations of these tensor components, where $d \neq 0$ leads to lobes at diagonal angles. In particular, we can also assign the angular pattern for the quadrupolar E_g and T_{2g} like modes.

DFT modeling based on the structural data reported in refs.[15,26] provides atomistic insight to the vibrational motions, as illustrated in Figure 4b. The isotropic A_{1g}-like modes correspond to symmetric stretching of the octahedra. The low frequency quadrupolar E_g-like modes can be

related to asymmetric octahedra stretching, and the T_{2g} modes Ag-Br or Bi-Br bond bending caused by an orthogonal motion of the Br ions. In the layered 2L-BA and 1L-BA structures, A_{1g}-like and E_g-like modes couple to motions of the organic spacer. The organic molecules bind to the octahedra lattice through hydrogen bonds with the Br ions, which facilitate the coupling of the vibrations of the inorganic lattice to the organic spacers.
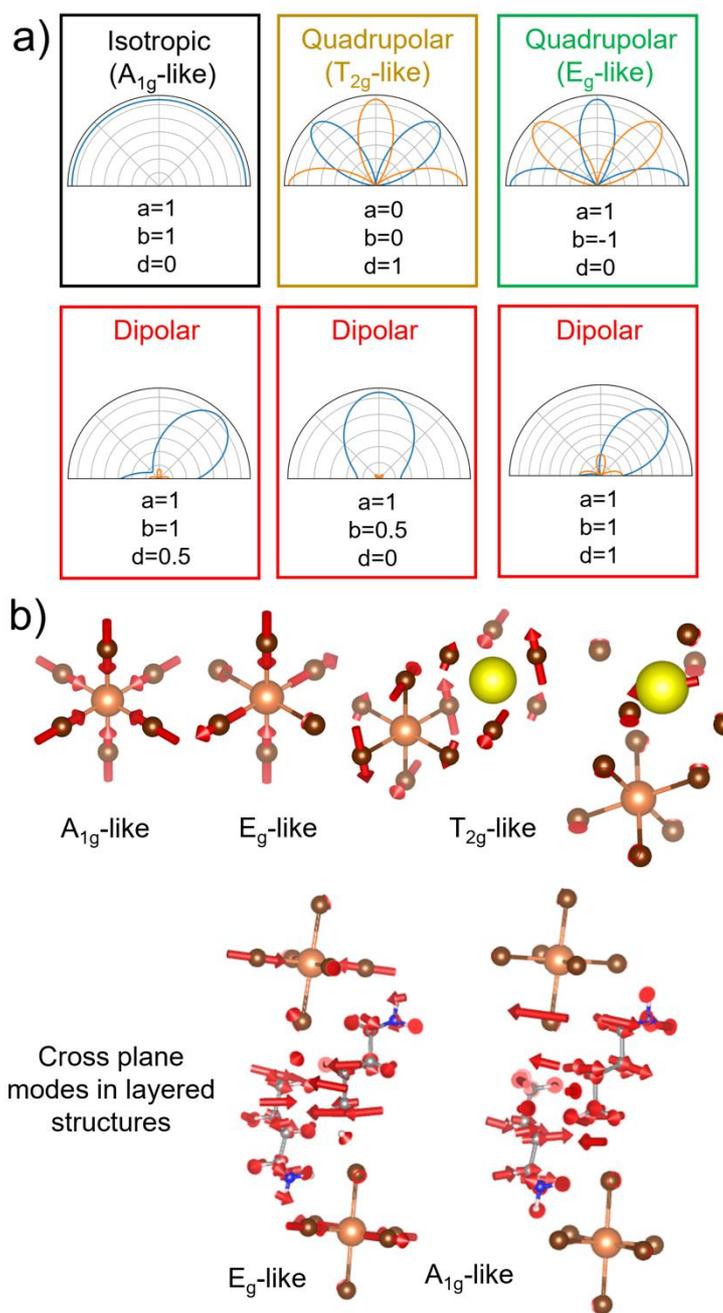

Figure 4. (a) Polar plots of the Raman mode calculated from the Raman tensor for selected values for its components. (b) Vibrational motions of the different modes obtained by DFT

modeling (only the sketches of the atoms involved in the main Raman modes are shown, see SI for the description of the rest of modes).

Figure 5 shows the color plot of the angle dependent Raman spectra (recorded at 30K and 300K) and polar plots for all observed modes of the 2L-BA sample ordered by symmetry and frequency for low and room temperature (see SI Figures S5 for the additional color plots of the Raman spectra). For the low-temperature monoclinic phase we observe isotropic (A_{1g}-like) character for the three low frequency modes and for the dominant high frequency modes at 146 and 173 cm^{-1}. The isotropic low-frequency modes result from octahedra stretching that involves the coupled motions of the Br$^-$ ions. The isotropic high frequency A_{1g}-like modes at 146 and 173 cm^{-1} stem from stretching of the octahedra cages, as evidenced by our DFT calculations (Figure 4b). This is in good agreement with the typical assignment of the strong mode at 173 cm^{-1} as an LO phonon mode with out-of-plane oscillation.[25,30] In the frequency range typical for metal cation-Br bond bending or stretching, from 60 to 140 cm^{-1}, we observe dipolar and quadrupolar modes with different directionality. Quadrupolar modes reflect the bidirectional symmetry of the octahedra lattice, and T_{2g}-like modes are strong along its diagonal directions, while the E_g-like mode is along the metal cation-Br bond directions. The E_g-like mode with relatively strong intensity originates from Ag-Br and Bi-Br bond stretching along the horizontal/vertical directions as evidenced by DFT (Figure 4b), which is also agrees with the direction of those bonds in the crystal structure in Figure 5b.

The directionality of the T_{2g}-like modes corresponds to the axes of the Cs ion sublattice; however, the T_{2g}-like modes involve also Ag-Br or Bi-Br bond bending as evidenced by our DFT modeling. The appearance of multiple modes should then result from different coupling between the sublattices.

The dipolar modes are induced by the preferential orientation of the organic molecules in the low temperature phase along one direction.[33] The butylammonium cations bind to the Br ions

in the inorganic octahedra lattice via hydrogen bonds,[47] which can induced static distortions, and facilitates coupling of the inorganic lattice modes to the organic molecules. Above the phase transition at RT the orientation of the molecules is changed and no dipolar modes are observed. The quadrupolar mode at 136 cm^{-1} maintains its E_g-like behavior at RT, evidencing that the crystallographic axis directions are not altered by the phase transition, in agreement with the interpretation that this phase transition is triggered by rearrangement of the organics.
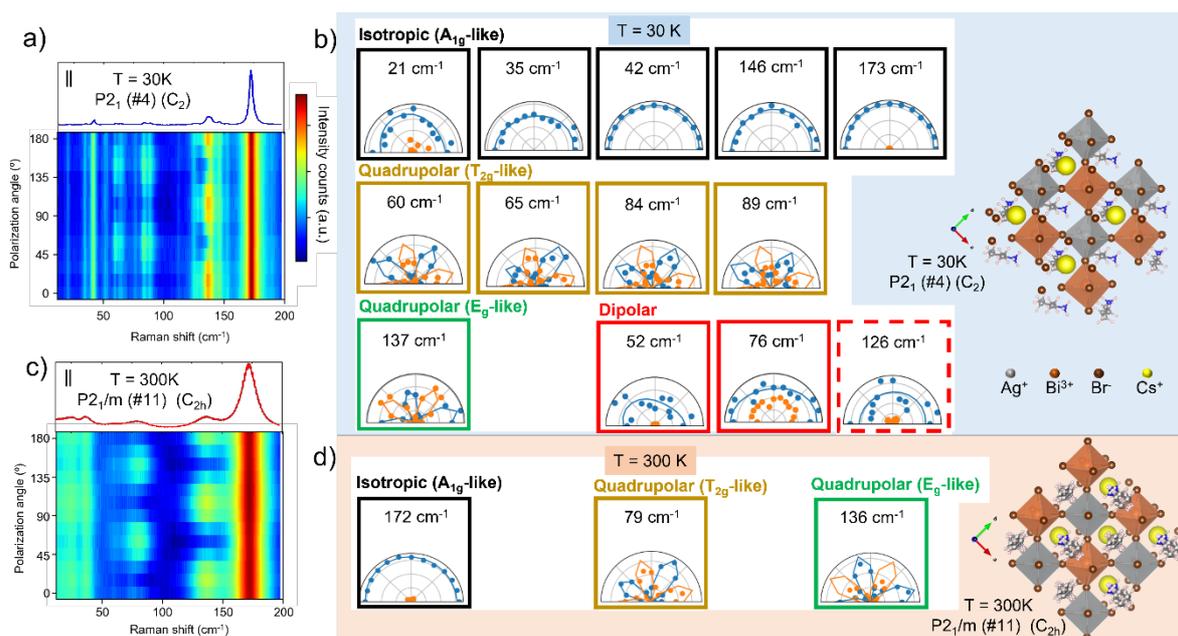

Figure 5. Angle dependence of the phonon modes of the 2L-BA sample: (a, c) Color plots of the polarized angle-dependent Raman spectra recorded at 30K and 300K, respectively (see Figure S5 in the SI for angle dependent Raman spectra in depolarized configuration). (b, d) Polar plots of the Raman mode intensities (dots) extracted from the data in Figure 5a,b and Figure S5, and best fits (lines) obtained from the corresponding Raman tensor equations. Polarized data is shown in blue, depolarized in orange. The top view on the crystal structure of the 2L sample at 30K and 300K using VESTA software[44] is also shown. The orientation of the principal axes in the octahedra plane is the same as in the polar plots.

Figure 6 shows the angular properties of the phonons in the 1L-BA sample. In the 1L-BA crystal structure at low temperature we notice a strong distortion of the in-plane angles, similar

to the lead-halide counterpart,[47,48] which is lifted at RT, where the in-plane angles are again close to 90°. In contrast to the 2L-BA sample where the low frequency modes were isotropic, here the modes at 24 and 42 cm^{-1} at low temperature are dipolar, which we attribute to the in-plane distortion of the octahedra lattice that affects the vibrations of the octahedra. Then at 64 and 66 cm^{-1} two more dipolar modes are observed that should stem from bond stretching in the inorganic lattice affected by the organic molecules, as discussed for the 2L-BA sample.

Two isotropic modes are identified: one at low frequency similar as in the 2L-BA sample, and one high frequency mode that results from out-of-plane oscillations and resembles the LO phonon mode. Furthermore, we observe four quadrupolar E_g-like modes that should originate from in-plane bond stretching, as in the other samples. The large number of the E_g-like modes can be associated to the distorted in-plane lattice.

Interestingly, we do not observe dominant T_{2g}-like modes in the 1L-BA sample, which strengthens our interpretation that these modes are related to the Cs-ion sublattice. And at RT we do not observe any dipolar modes, which is caused by the phase transition that leads to a disordered (liquid-like) phase of the organic cations, and almost orthogonal in-plane angles in the inorganic lattice.
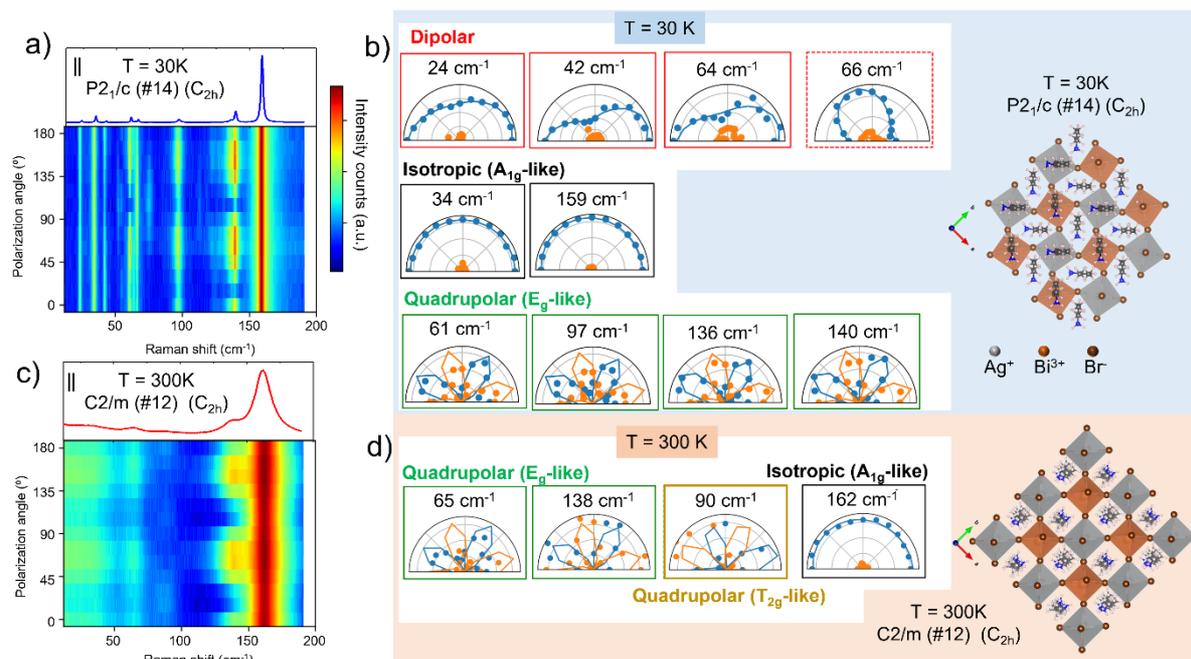
Figure 6. Angle dependence of the phonon modes of the 1L-BA sample: (a, c) Color plots of polarized-dependent Raman spectra at 30K and 300K, respectively, (see Figure S6 in the SI for angle dependent Raman spectra in depolarized configuration). (b) Polar plots of the Raman mode intensities (dots) extracted from the data in Figure 6a,b and Figure S6, and best fits (lines) obtained from the corresponding Raman tensor equations. Polarized data is shown in blue, depolarized in orange. The top view on the crystal structure of the 1L sample at 30K and 300K using VESTA software[44] is also displayed. The orientation of the principal axes in the octahedra plane is the same as for the polar plots.

Finally, we discuss the temperature dependent behavior of the Raman modes displayed in **Table 1**. As shown in **Figure 7**, for the 3D structure, we determine the phase transition temperature from tetragonal to cubic at 110-150K, in good agreement with the 122 K obtained by XRD, absorbance and heat capacity results reported in literature.[26] This is most evident for the dipolar low-frequency mode that redshift with increasing temperature towards the phase transition, and finally quenches at the transition temperature. This is the behavior of a soft mode. Similarly, for the 2L-BA sample, we find a phase transition temperature of ~200K (Figure 7) from the dependence of the T_{2g}-like mode at 90 cm^{-1} that also is not present above the phase

transition temperature. This transition was still not established in literature, although expected from XRD results in the range 100-300K.[15] In the 1L-BA case, the transition is clearly marked by an abrupt shift of the mode frequencies at 282 K, in accordance with our previous results for the modes at 140 and 160 cm^{-1}.[33] We note that the mode at 90 cm^{-1} changes character at the phase transition, from E_g-like feature at low temperature to T_{2g}-like feature at high temperature, and that this transition leads to a decrease in frequency, while for all other modes the transition to the high temperature phase leads to a blue-shift.

The fact that we observe gradual or abrupt changes of the frequencies of certain Raman modes at the phase transition allows us to distinguish first and second order phase transitions. The discontinuous change in frequency of the A_{1g} mode at 160 cm^{-1} and E_g mode at 60 cm^{-1} in the 1L-BA sample clearly identifies a first order phase transition, where the crystal lattice changes configuration. This is in agreement with the XRD results[15] from which Figure 7 was derived. The continuous change in frequency of the A_{1g}-like and other modes in the 2L-BA and 3D sample point to a second order transition, where only the organic molecule conformation changes from an ordered to a disordered phase.

Table 1. Main low-frequency (< 200 cm^{-1}) Raman peaks observed for the $Cs_2AgBiBr_6$ crystal, $(BA)_2CsAgBiBr_7$ 2L flakes, and $(BA)_4AgBiBr_8$ 1L flakes at low (30K) and room temperature (300K) with the corresponding crystal structures, symmetry, and the correlation among the experimentally observed vibrational modes and angular patterns (isotropic – I, quadrupolar – Q and dipolar – D) (see SI for more details).

3D (Tetragonal I4/m, #87) (30K)			2L-BA (Monoclinic P2₁, #4) (30K)			1L-BA (Monoclinic P2₁/c, #14) (30K)		
Exp. Raman Shift (cm^{-1})	Angular pattern	Symmetry	Exp. Raman Shift (cm^{-1})	Angular pattern	Symmetry	Exp. Raman Shift (cm^{-1})	Angular pattern	Symmetry
29	D	E_g	21	I	A	24	D	A_g
40	Q	B_g	35	I	A	34	I	A_g
45	D	B_g	42	I	A	42	D	A_g
-	-	-	65	Q	A	61	Q	A_g

73	Q	E_g	-	-	-	-	-	-
-	-	-	84	Q	A	-	-	-
-	-	-	89	Q	A	-	-	-
-	-	-				97	Q	A_g
140	Q	B_g	137	Q	A	140	Q	A_g
180	I	A_g	172	I	A	159	I	A_g

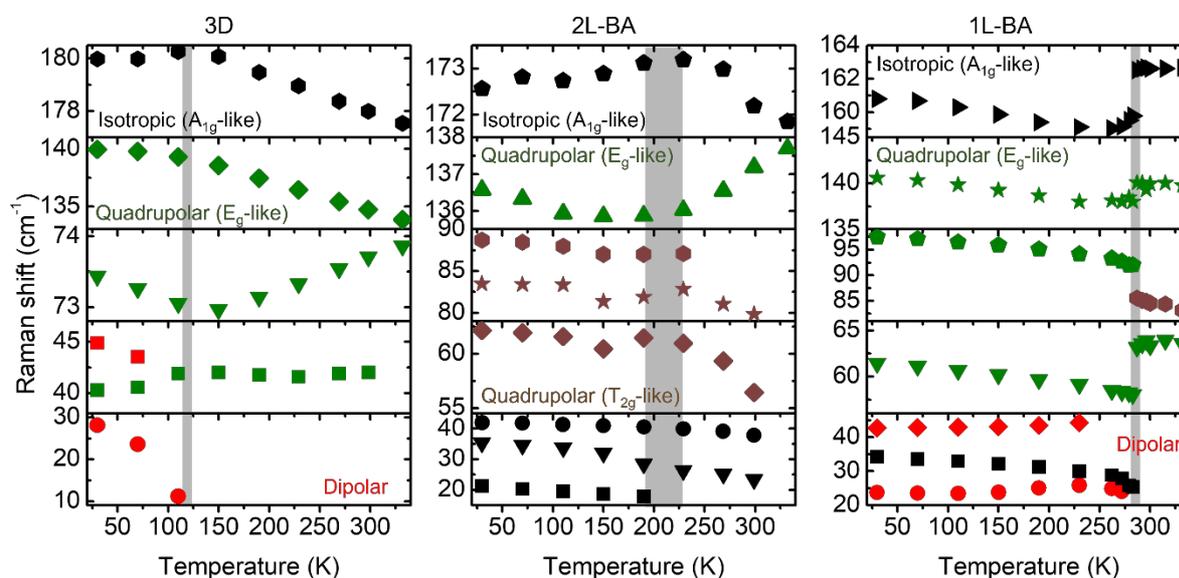| 3D (Cubic Fm-3m, #225) (300K)			2L-BA (Monoclinic P2$_1$/m, #11) (300 K)			1L-BA (Monoclinic C2/m, #12) (300 K)		
Exp. Raman Shift (cm^{-1})	Angular pattern	Symmetry	Exp. Raman Shift (cm^{-1})	Angular pattern	Symmetry	Exp. Raman Shift (cm^{-1})	Angular pattern	Symmetry
-	-	-	31	I	A_g	-	-	-
39	Q	T_{2g}	38	I	A_g	35	I	A_g
-	-	-	62	Q	A_g	65	D	A_g
75	Q	T_{2g}	79	Q	A_g	-	-	-
-	-	-	-	-	-	90	Q	A_g
135	Q	E_g	136	Q	A_g	138	Q	A_g
175	I	A_{1g}	172	I	A_g	162	I	A_g

Figure 7. Temperature dependence of the Raman shift of the dominant Raman modes for the 3D crystal and 2L-BA and 1L-BA flakes. The data was collected from the polarized (∥) and depolarized (⊥) configurations.

In conclusion, we presented a comprehensive study of the Raman active vibrational modes in double perovskites with Ag and Bi as metal cations, including DFT modeling and point group symmetries. We demonstrated that angle-dependent polarized Raman spectroscopy is a versatile tool to experimentally access the directionality and symmetry of the fundamental

phonon modes of the (low-dimensional layered) perovskite crystals. Our study elucidated the coupling between the organic cations and the inorganic octahedra in the layered structures, and revealed the sensitivity of the low-frequency modes to the phase transitions of the crystal lattice. In this respect, we discovered a secondary phase transition that is determined by the rearrangement of the organic cations coupled to the octahedra layer and which shifts to higher temperature with the reduction of the number of octahedral layers. Therefore, our work provides very interesting information regarding the temperature dependent phase transitions in metal-halide perovskites. We show that both the frequency and the symmetry of the phonon mode can be affected by the phase transition, which provides detailed insights into the nature of the phase transition, i.e. if it is first or second order, and the properties of the affected phonon mode can also elucidate what processes trigger such transitions.

Such insights are highly valuable to understand thermal and optoelectronic properties of such materials. For example, light emission is strongly affected by electron-phonon coupling in this family of double perovskite, caused by the extremely flat dispersion of the conduction band edge.[33] This leads to a strong influence of the lattice distortions and phonon coupling on the emission wavelength, and indeed, for 3D perovskites and 2L structures the band gap is indirect and red light emission is caused by radiative defects, while for 1L structures the band gap is direct around 3 eV, leading to deep blue light emission. Interestingly, the photoluminescence spectra of the 1L samples feature weaker broad emission bands in the visible spectral range, which resemble the self-trapped exciton (STE) emission that is well known for lead halide layered perovskites. STE emission is strongly related to electron-phonon coupling, and our study indicates that similar coupling mechanism should be at work in the double perovskites. This knowledge opens the way to design lead-free materials for white light emission.

Supporting Information

Experimental methods; DFT calculations; 3D crystal orientation; Additional Raman and structural data analysis; Angle variation study; Phase transition determination. Supporting Information is available free of charge from the Wiley Online Library.

Acknowledgements

(† B.M-G. and D.S. contributed equally to this work.)

Received: ((will be filled in by the editorial staff))
Revised: ((will be filled in by the editorial staff))
Published online: ((will be filled in by the editorial staff))

References

[1] B. Vargas, G. Rodríguez-López, D. Solis-Ibarra, *ACS Energy Lett.* **2020**, *5*, 3591.

[2] H. Lei, D. Hardy, F. Gao, *Adv. Funct. Mater.* **2021**, 2105898.

[3] E. Greul, M. L. Petrus, A. Binek, P. Docampo, T. Bein, *J. Mater. Chem. A* **2017**, *5*, 19972.

[4] M. Wang, P. Zeng, S. Bai, J. Gu, F. Li, Z. Yang, M. Liu, *Sol. RRL* **2018**, *2*, 1800217.

[5] M. Pantaler, K. T. Cho, V. I. E. Queloz, I. García Benito, C. Fettkenhauer, I. Anusca, M. K. Nazeeruddin, D. C. Lupascu, G. Grancini, *ACS Energy Lett.* **2018**, *3*, 1781.

[6] F. Igbari, R. Wang, Z.-K. Wang, X.-J. Ma, Q. Wang, K.-L. Wang, Y. Zhang, L.-S. Liao, Y. Yang, *Nano Lett.* **2019**, *19*, 2066.

[7] Z. Zhang, C. Wu, D. Wang, G. Liu, Q. Zhang, W. Luo, X. Qi, X. Guo, Y. Zhang, Y. Lao, B. Qu, L. Xiao, Z. Chen, *Org. Electron.* **2019**, *74*, 204.

[8] C. Wu, Q. Zhang, Y. Liu, W. Luo, X. Guo, Z. Huang, H. Ting, W. Sun, X. Zhong, S. Wei, S. Wang, Z. Chen, L. Xiao, *Adv. Sci.* **2018**, *5*, 1700759.

[9] X. Yang, W. Wang, R. Ran, W. Zhou, Z. Shao, *Energy Fuels* **2020**, *34*, 10513.

[10] J. Yang, C. Bao, W. Ning, B. Wu, F. Ji, Z. Yan, Y. Tao, J. Liu, T. C. Sum, S. Bai, J. Wang, W. Huang, W. Zhang, F. Gao, *Adv. Opt. Mater.* **2019**, 1801732.

[11] F. Fang, H. Li, S. Fang, B. Zhou, F. Huang, C. Ma, Y. Wan, S. Jiang, Y. Wang, B. Tian, Y. Shi, *Adv. Opt. Mater.* **2021**, *9*, 2001930.

[12] W. Pan, H. Wu, J. Luo, Z. Deng, C. Ge, C. Chen, X. Jiang, W.-J. Yin, G. Niu, L. Zhu, L. Yin, Y. Zhou, Q. Xie, X. Ke, M. Sui, J. Tang, *Nat. Photonics* **2017**, *11*, 726.

[13] X. Cheng, W. Qian, J. Wang, C. Yu, J. He, H. Li, Q. Xu, D. Chen, N. Li, J. Lu, *Small* **2019**, *15*, 1905731.

[14] Z. Liu, H. Yang, J. Wang, Y. Yuan, K. Hills-Kimball, T. Cai, P. Wang, A. Tang, O. Chen, *Nano Lett.* **2021**, *21*, 1620.

[15] B. A. Connor, L. Leppert, M. D. Smith, J. B. Neaton, H. I. Karunadasa, *J. Am. Chem. Soc.* **2018**, *140*, 5235.

[16] L. Mao, S. M. L. Teicher, C. C. Stoumpos, R. M. Kennard, R. A. DeCrescent, G. Wu, J. A. Schuller, M. L. Chabinyc, A. K. Cheetham, R. Seshadri, *J. Am. Chem. Soc.* **2019**, *141*, 19099.

[17] Y. Fang, L. Zhang, L. Wu, J. Yan, Y. Lin, K. Wang, W. L. Mao, B. Zou, *Angew. Chem. Int. Ed.* **2019**, *58*, 15249.

[18] E. T. McClure, A. P. McCormick, P. M. Woodward, *Inorg. Chem.* **2020**, *59*, 6010.

[19] F. Schmitz, J. Horn, N. Dengo, A. E. Sedykh, J. Becker, E. Maiworm, P. Bélteky, Á. Kukovecz, S. Gross, F. Lamberti, K. Müller-Buschbaum, D. Schlettwein, D. Meggiolaro, M. Righetto, T. Gatti, *Chem. Mater.* **2021**, *33*, 4688.

[20] S.-Y. Kim, J.-M. Yang, S.-H. Lee, N.-G. Park, *Nanoscale* **2021**, *13*, 12475.

[21] Z. Xu, X. Liu, Y. Li, X. Liu, T. Yang, C. Ji, S. Han, Y. Xu, J. Luo, Z. Sun, *Angew. Chem. Int. Ed.* **2019**, *58*, 15757.

[22] W. Guo, X. Liu, S. Han, Y. Liu, Z. Xu, M. Hong, J. Luo, Z. Sun, *Angew. Chem.* **2020**, *132*, 13983.

[23] W. Zhang, M. Hong, J. Luo, *Angew. Chem. Int. Ed.* **2020**, *59*, 9305.

[24] Y. Li, T. Yang, Z. Xu, X. Liu, X. Huang, S. Han, Y. Liu, M. Li, J. Luo, Z. Sun, *Angew. Chem. Int. Ed.* **2020**, *59*, 3429.

[25] S. J. Zelewski, J. M. Urban, A. Surrente, D. K. Maude, A. Kuc, L. Schade, R. D. Johnson, M. Dollmann, P. K. Nayak, H. J. Snaith, P. Radaelli, R. Kudrawiec, R. J. Nicholas, P. Plochocka, M. Baranowski, *J. Mater. Chem. C* **2019**, *7*, 8350.

[26] L. Schade, A. D. Wright, R. D. Johnson, M. Dollmann, B. Wenger, P. K. Nayak, D. Prabhakaran, L. M. Herz, R. Nicholas, H. J. Snaith, P. G. Radaelli, *ACS Energy Lett.* **2019**, *4*, 299.

[27] J. Su, T. Mou, J. Wen, B. Wang, *J. Phys. Chem. C* **2020**, *124*, 5371.

[28] A. Schmitz, L. L. Schaberg, S. Sirotinskaya, M. Pantaler, D. C. Lupascu, N. Benson, G. Bacher, *ACS Energy Lett.* **2020**, *5*, 559.

[29] A. Dey, A. F. Richter, T. Debnath, H. Huang, L. Polavarapu, J. Feldmann, *ACS Nano* **2020**, *14*, 5855.

[30] J. A. Steele, P. Puech, M. Keshavarz, R. Yang, S. Banerjee, E. Debroye, C. W. Kim, H. Yuan, N. H. Heo, J. Vanacken, A. Walsh, J. Hofkens, M. B. J. Roeffaers, *ACS Nano* **2018**, *12*, 8081.

[31] A. H. Slavney, T. Hu, A. M. Lindenberg, H. I. Karunadasa, *J. Am. Chem. Soc.* **2016**, *138*, 2138.

[32] P. Pistor, M. Meyns, M. Guc, H.-C. Wang, M. A. L. Marques, X. Alcobé, A. Cabot, V. Izquierdo-Roca, *Scr. Mater.* **2020**, *184*, 24.

[33] B. Martín-García, D. Spirito, G. Biffi, S. Artyukhin, Francesco Bonaccorso, R. Krahne, *J. Phys. Chem. Lett.* **2021**, *12*, 280.

[34] C. Quarti, G. Grancini, E. Mosconi, P. Bruno, J. M. Ball, M. M. Lee, H. J. Snaith, A. Petrozza, F. De Angelis, *J. Phys. Chem. Lett.* **2014**, *5*, 279.

[35] A. M. A. Leguy, A. R. Goñi, J. M. Frost, J. Skelton, F. Brivio, X. Rodríguez-Martínez, O. J. Weber, A. Pallipurath, M. I. Alonso, M. Campoy-Quiles, M. T. Weller, J. Nelson, A. Walsh, P. R. F. Barnes, *Phys. Chem. Chem. Phys.* **2016**, *18*, 27051.

[36] T. Yin, Y. Fang, X. Fan, B. Zhang, J.-L. Kuo, T. J. White, G. M. Chow, J. Yan, Z. X. Shen, *Chem. Mater.* **2017**, *29*, 5974.

[37] Y. Guo, O. Yaffe, D. W. Paley, A. N. Beecher, T. D. Hull, G. Szpak, J. S. Owen, L. E. Brus, M. A. Pimenta, *Phys. Rev. Mater.* **2017**, *1*, 042401.

[38] J. Ibaceta-Jaña, R. Muydinov, P. Rosado, H. Mirhosseini, M. Chugh, O. Nazarenko, D. N. Dirin, D. Heinrich, M. R. Wagner, T. D. Kühne, B. Szyszka, M. V. Kovalenko, A. Hoffmann, *Phys. Chem. Chem. Phys.* **2020**, *22*, 5604.

[39] C. M. Mauck, A. France-Lanord, A. C. Hernandez Oendra, N. S. Dahod, J. C. Grossman, W. A. Tisdale, *J. Phys. Chem. C* **2019**, *123*, 27904.

[40] N. S. Dahod, A. France-Lanord, W. Paritmongkol, J. C. Grossman, W. A. Tisdale, *J. Chem. Phys.* **2020**, *153*, 044710.

[41] B. Dhanabalan, Y.-C. Leng, G. Biffi, M.-L. Lin, P.-H. Tan, I. Infante, L. Manna, M. P. Arciniegas, R. Krahne, *ACS Nano* **2020**, *14*, 4689.

[42] M. Menahem, Z. Dai, S. Aharon, R. Sharma, M. Asher, Y. Diskin-Posner, R. Korobko, A. M. Rappe, O. Yaffe, *ACS Nano* **2021**, *15*, 10153.

[43] Miao-Ling Lin, Balaji Dhanabalan, Giulia Biffi, Yu-Chen Leng, Seda Kutkan, Milena P. Arciniegas, Ping-Heng Tan, Roman Krahne, *Small* **2022**, *just accepted manuscript*.

[44] K. Momma, F. Izumi, *J. Appl. Crystallogr.* **2011**, *44*, 1272.

[45] M. A. Pérez-Osorio, Q. Lin, R. T. Phillips, R. L. Milot, L. M. Herz, M. B. Johnston, F. Giustino, *J. Phys. Chem. C* **2018**, *122*, 21703.

[46] X.-L. Liu, X. Zhang, M.-L. Lin, P.-H. Tan, *Chin. Phys. B* **2017**, *26*, 067802.

[47] B. Dhanabalan, G. Biffi, A. Moliterni, V. Olieric, C. Giannini, G. Saleh, L. Ponet, M. Prato, M. Imran, L. Manna, R. Krahne, S. Artyukhin, M. P. Arciniegas, *Adv. Mater.* **2021**, *33*, 2008004.

[48] X. Gong, O. Voznyy, A. Jain, W. Liu, R. Sabatini, Z. Piontkowski, G. Walters, G. Bappi, S. Nokhrin, O. Bushuyev, M. Yuan, R. Comin, D. McCamant, S. O. Kelley, E. H. Sargent, *Nat. Mater.* **2018**, *17*, 550.

The table of contents entry should be 50–60 words long and should be written in the present tense. The text should be different from the abstract text.

Single flakes of layered low-dimensional perovskites can be mechanically exfoliated such that their octahedra lattice planes are parallel to the substrate surface. This enables a detailed mapping of the directionality of the vibrational modes of the inorganic lattice by polarized Raman spectroscopy. Here, a detailed study of the basic phonon modes in double perovskites supported by density functional and group theory is presented.

Low-frequency phonon modes in layered double perovskites: symmetry, polarity, and relation to phase transitions

Beatriz Martín-García*†, Davide Spirito*†, Miao-Ling Lin, Yu-Chen Leng, Sergey Artyukhin, Ping-Heng Tan, Roman Krahne*

ToC figure ((Please choose one size: 55 mm broad × 50 mm high **or** 110 mm broad × 20 mm high. Please do not use any other dimensions))